Microstructural features in additively manufactured EUROFER97 components

Simon Bonk[a,], Michael Dürrschnabel [a], Heiko Neuberger[b], Esther Simondon[a], Michael Rieth[a]*

a: Karlsruhe Institute of Technology, Institute for Applied Materials, 76344 Eggenstein-Leopoldshafen, Germany
b: Karlsruhe Institute of Technology, Institute for Neutron Physics and Reactor Technology, 76344 Eggenstein-Leopoldshafen, Germany

Corresponding author:
*: Simon Bonk, Karlsruhe Institute of Technology (KIT), Institute for Applied Materials (IAM-AWP), Hermann-von-Helmholtz-Platz 1, 76344 Eggenstein-Leopoldshafen, Germany, Phone: +49 721 608 26402, E-Mail: simon.bonk@kit.edu

Simon Bonk	simon.bonk@kit.edu
https://orcid.org/0000-0002-5722-2005	
Michael Dürrschnabel	michael.duerrschnabel@kit.edu
https://orcid.org/0000-0002-9047-6541	
Heiko Neuberger	heiko.neuberger@kit.edu
https://orcid.org/0000-0001-6915-9544	
Michael Rieth	michael.rieth@kit.edu
https://orcid.org/0000-0002-6231-6241	
Esther Simondon	esther.simondon@kit.edu
https://orcid.org/0000-0002-8094-281X	

Abstract

By uncoupling the manufacturability from the design process, additive manufacturing of RAFM steels like EUROFER97 can open significant design freedom for components in fusion reactors, e.g., breeding blankets and divertor applications.
As mechanical properties of RAFM steels are based on their specific microstructure and high number density of precipitates, good control of the microstructure of additively manufactured parts has to be ensured. As additive manufactured components are known to possess unique microstructures compared to EUROFER97 from standard technologies, the aim of this paper is to investigate additive manufactured EUROFER97 components and the influence of post-processing steps on their microstructure and in particular on the formation of precipitates.
This paper covers the technological fabrication process of EUROFER97 by selective laser melting (SLM), including the production and chemical analysis of pre-alloyed EUROFER97 powder. In the initial state after fabrication, SLM-EUROFER97 components exhibit a bimodal, anisotropic microstructure with large ferritic grains instead of the desired homogeneous, fully martensitic microstructure. Further, neither $M_{23}C_6$ nor MX precipitates were detected in the as-built condition. A heat treatment including hot isostatic pressing, austenitization, quenching and tempering, allows achieving a fully martensitic, uniform microstructure as well as the formation of $M_{23}C_6$ and MX precipitates with similar size and volume density as in conventionally produced EUROFER97. In combination with the chemical analysis of the raw material, impurities stemming from the atomization process forming oxides were detected. However, due to their small size, those are not expected to influence the performance of SLM-processed EUROFER97. The comparison of the as-built condition and the condition after hot isostatic pressing and heat treatments reveals the necessity of appropriate post-processing to tailor the microstructure to one comparable to conventional EUROFER97.

Keywords

- Additive manufacturing
- Selective Laser Melting
- 9Cr-1W-V-Ta steel
- $M_{23}C_6$ precipitates
- MX precipitates
- Martensitic microstructure

1. Introduction

Additive manufacturing (AM) is often referred to as a “disruptive technology” [1] because it offers revolutionary ways of designing components by uncoupling the manufacturability from the design process.
Due to the novelty of the technique, especially regarding the AM of structural materials for high heat flux and nuclear applications, the engineering and design rules are yet to be determined.
This paper will focus on industrially available state-of-the-art additive manufacturing by powder-bed selective laser melting (SLM). Earlier SLM studies produced breeding-blanket and first wall components (typical nuclear fusion applications) of P91 [2], 316L [3] and EUROFER97 [4,5] steels. These studies demonstrated the feasibility of the SLM technique in combination with hot isostatic pressing (HIP) from an engineering point of view to produce fusion related steel parts with complex geometry in one production step. This study will focus on steel grade EUROFER97, a reduced activation ferritic-martensitic (RAFM) steel as a baseline material for test blanket modules in ITER and presumably for most components in DEMO [6].
To utilize additive manufactured RAFM steels for breeding blanket or divertor applications, it is not only necessary to control the SLM-processes sufficiently to meet the engineering requirements regarding the dimensional accuracy, but also to ensure sufficient performance from a materials science point of view. To meet the design code requirements for structural materials in fusion reactor applications, especially under neutron irradiation, it is important to ensure a similar performance in key mechanical properties of EUROFER97 processed by SLM in comparison to conventionally produced EUROFER97.
Mechanical properties of RAFM steels are linked to their specific microstructure, i.e. a fine martensite lath structure and high number density of precipitates in form of $M_{23}C_6$ (M = Cr, W) and MX (V-,Ta-rich ntrides) [7]. Hence, a good control of the microstructure of additively manufactured parts has to be ensured - if necessary by tailoring undesired microstructures with appropriate heat treatments.
This is of particular importance when considering the repeated remelting of the top layers during SLM processing, the high thermal gradients and the dependence of these thermal gradients on geometrical feature sizes, as the microstructure develops simultaneously with the geometry during SLM [8,9]. These circumstances are known to result in unique microstructures for SLM-parts, which are difficult to predict because simulations have to combine models with different length scales [10].

Therefore, this study will address the following questions:

(1) What are the microstructural characteristics of EUROFER97 processed by SLM concerning grain size and shape?
(2) Do both M23C6 and MX type precipitates form homogeneously distributed in EUROFER97 processed by SLM?
(3) If necessary, how can the microstructure be altered to one comparable to the microstructure of conventionally fabricated EUROFER97?

To address these questions, the paper is organized as follows: first, the fabrication steps from powder atomization over the SLM production to the post-processing are described to allow a discussion on the influence of the respective fabrication steps on the resulting microstructure and precipitates. Then, the description of the experiments is presented, comprising the chemical analysis of the raw material, the atomized powder and the final SLM parts, as well as microstructural analyses of grain size and shape by EBSD, and size and distribution of precipitates by TEM. EBSD and TEM were performed on EUROFER97 in the initial state after SLM and after post-processing. Post-processing of the SLM-parts includes hot isostatic pressing (HIP) followed by heat treatment (austenitization, quenching, tempering).

2. Material and fabrication

2.1. Powder production

For the discussion of microstructural features of RAFM steels fabricated by additive manufacturing, this study employs EUROFER97 steel grade, which serves as a baseline material for test blanket modules in ITER and presumably the whole breeding blanket in DEMO [6]. All components for this study have been fabricated by powder-bed selective laser melting (SLM) as an industrially available state-of-the-art additive manufacturing technique.

The production of EUROFER97 powder suitable for additive manufacturing was realized by atomization under inert gas atmosphere, using a EUROFER97 steel plate for atomization to produce pre-alloyed powder, as already demonstrated for different steels [11–13]. The process parameters during atomization were optimized to achieve spherical powder particles with a high yield in the target fraction between 10 µm and 45 µm to guarantee a sufficient flowability of the powder. The atomization resulted in a yield of 60 % in the target fraction and the flowrate of 16.03 s/50g in standard Hall flow tests (DIN EN ISO 4490) confirmed the flowability of the powder. Details on the production of the powder batches can be found in an earlier publication [14].

Even though both the powder production and the SLM process are conducted under an inert gas atmosphere (argon), the atmospheres in these industrial machines are not expected to be free of impurities. The chemical composition regarding the main elements of the powder and the components fabricated from these powders, as well as the reference alloy and EUROFER97 specifications are summarized in Tab. 1. The complete analysis can be found in the supplementary material (Tab. S 1). The impact of the chemical composition on various properties of RAFM steels was studied in [15–21].

The chromium concentration was increased on purpose during atomization to reach a concentration similar to the reference material. However, the pre-alloyed powder shows some further notable differences compared to the raw material as well as to the reference material (EUROFER_Ref) and EUROFER97 specifications: the content of manganese is below specifications and the nitrogen content is reduced in comparison to the raw material, while vanadium, boron and oxygen contents are above specifications. Further, aluminium concentration in the EUROFER97 powder is higher than in the raw material and the reference specimen.

The decreased amount of manganese and the increased amount of vanadium is due to the EUROFER97 steel plate from an experimental EUROFER97 batch used for atomization, which itself had the same low amount of manganese and increased amount of vanadium. However, due to the purity of the EUROFER97 steel grade (low amount of sulfur), a low manganese content should have no notable influence on microstructure or mechanical properties. The increased aluminum and boron contents, however, can be attributed to the atomization processes, either due to impurities from earlier batches or, in case of boron, due to abrasions from the boron-nitride nozzle used during the atomization process. The contamination with aluminum is still below the limits specified for EUROFER97, but in case of boron, the contamination is significantly above the specifications. As the specifications not only set a maximum boron content of 0.001 wt.-% but also urge to keep the boron concentration as low as possible, such contamination has to be avoided. For further production of EUROFER97 powder suitable for additive manufacturing by this fabrication route, the authors suggest using a boron-free ceramic nozzle. Further, the powder exhibits an increased oxygen content after atomization, which can be attributed to impurities in the argon atmosphere of this industrial-scale process.

Tab. 1: Chemical composition (wt.-%) of raw material, produced pre-alloyed powder and SLM parts fabricated with this powder. For comparison, the chemical composition (wt.-%) of the reference material (EUROFER_Ref) and the EUROFER97 specifications (EUROFER_Spec) are given.

(wt.-%)	Cr	C	Mn	V	W	Ta	N	O	B	Al	S
raw material	8.73	0.11	0.019	0.35	1.08	0.092	0.042	0.0052	$< 5 \cdot 10^{-4}$	0.0014	0.0011
pre-alloyed powder	9.46	0.1	0.021	0.35	1.10	0.090	0.025	0.022	0.017	0.0037	$<2 \cdot 10^{-3}$
SLM parts	9.39	0.09	0.019	0.36	1.12	0.094	0.0254	0.0065	0.017	0.0034	$<2 \cdot 10^{-3}$
EUROFER_Ref	9.36	0.095	0.501	0.19	1.21	0.1	0.041	0.0104	/	<0.001	0.0017
EUROFER97_Spec	8.5-9.5	0.09-0.12	0.2-0.6	0.15-0.25	1.0-1.2	0.05-0.09	0.015-0.045	< 0.01	< 0.001	< 0.01	< 0.005

2.2. Selective Laser Melting

The SLM fabrication was performed by Rosswag GmbH with an SLM280HL Twin machine from SLM Solutions. To minimize the influence of the SLM process peripherals on the chemical composition, especially on the first layers, a building plate made of P92 (steel with a composition similar to EUROFER97) was installed, and the sieves used for the powder handling were exclusively deployed during the fabrication of the SLM-EUROFER components.
The SLM fabrication of EUROFER97 components was optimized in terms of volumetric energy density [22] in a way to achieve complete melting of the powder as well as low porosity of the final part. The parameter set yielding the lowest porosity of 0.49% consists, regarding the most crucial parameters, in a laser power of 200 W, layer height of 30 µm, scan velocity of 800 mm/s and hatch distance of 80 µm. These parameters result in a volumetric energy density of 104 J/mm^3. As scanning strategy, a chessboard pattern with 67° rotation between layers was applied. To reduce the cooling gradient and with it the thermally induced stress, the SLM fabrication was performed with a building plate temperature of 200°C. For the investigation of the bulk microstructure of EUROFER97 processed by SLM, blocks of 40 mm x 40 mm x 11 mm have been fabricated to analyze the microstructural features of SLM-EUROFER independently of the geometry.

2.3. Post-processing

Even if SLM components can be fabricated with a sufficient density, metal parts produced by SLM are known to exhibit unique microstructures, as the geometry and the microstructure develop simultaneously during production, unlike for conventional fabrication methods [23,24]. Post-processing by hot isostatic pressing (HIP) and subsequent heat treatments were performed on the SLM batches with the intent to achieve a EUROFER97 like microstructure with low porosity. To separate the influence of SLM production and possible improvements by post-processing, both batches were analysed and tested in their as-built condition (SLM-EUROFER), as well as after post-processing (SLM-EUROFER_HT). Post-processing parameters have been chosen based on experience with EUROFER97-type steels [25,26]. Only the tempering temperature of 750 °C was chosen lower as the 780 °C used for the conventionally produced reference material (EUROFER_Ref) to be safely below the alpha-gamma transformation temperature. But this difference should not be relevant for the formation of precipitates, which are the focus of this publication.

Details on the volumetric energy density, post-processing parameters and porosity can be found in Tab. 2, including the reference materials produced by conventional melting-based metallurgy and thermomechanical processing.

Tab. 2: Fabrication, post-processing parameters and residual porosity (measured by Archimedes principle) of SLM parts produced for this study and the reference material chosen for comparison.

	fabrication	HIP	heat treatment	porosity
SLM-EUROFER	SLM E_V = 104 J/mm^3	/	/	0.49%
SLM-EUROFER_HT	SLM E_V = 104 J/mm^3	100 bar 1000°C	980°C / 30 min + 750°C / 2 h	0.12%
EUROFER_Ref	casting, hot rolling, water quenching	/	980°C / 30 min + 780°C / 2 h	/

3. Experimental

3.1. Microstructural Analysis: EBSD

Microstructure investigations were performed with a Zeiss Merlin field-emission-gun scanning electron microscope (SEM) equipped with an EDAX Hikari high-speed electron backscatter diffraction (EBSD) camera. The build direction during the SLM process, which is the direction perpendicular to the powder layers, served as the reference axis. Accordingly, measurements perpendicular to the build direction display a multitude of powder layers.
The EBSD analysis was performed on areas of 100 µm x 80 µm, scanned with a step size of 200 nm using an acceleration voltage of 20 kV and a probe current of 10 nA. Points with a confidence index (CI) lower than 0.1 were removed during post-processing. Apart from a Grain CI Standardization, no clean-up of the datasets was performed and therefore the orientations of the data points remained unchanged.
The depiction of the microstructure from the EBSD datasets is performed by inverse pole figure maps (IPF). For the quantitative analysis, high-angle boundaries with misorientations exceeding 15° were considered as grain boundaries.

3.2. Microstructural Analysis (precipitates): Transmission electron microscopy

TEM characterization was performed in a Thermofisher Talos F200X scanning transmission electron microscope (STEM) operated at 200 kV and equipped with four energy-dispersive X-ray (EDX) detectors and a Gatan Enfinium electron energy-loss (EEL) spectrometer with DualEELS capability. The STEM-EDX mappings were acquired using spot size setting No. 6. The convergence angle of the electron probe was 10.5 mrad.
Grain size evaluation of both the $M_{23}C_6$ and MX-type phase was carried out using ImageJ. In case of the $M_{23}C_6$, two 8.825 µm x 8.825 µm sized Cr-K_α elemental maps were thresholded and Feret's diameter was determined as measure for the precipitate size. For the MX-type phases, the map sizes were reduced to 3.12 µm x 3.12 µm to improve the lateral resolution. However, in the case of the MX phases data evaluation is more complex. At least the Ta and V elemental maps need to be evaluated with respect to the size of these precipitates, since the MX-type particles involve both elements. For a detailed understanding of the involved phases, a principal component analysis (PCA) of a STEM-EDX dataset was carried out using the non-negative matrix

factorization algorithm in order to obtain physically meaningful data. The EDX data was normalized with respect to Poisson noise prior to PCA. PCA was carried out using the Hyperspy program package [27].

4. Results and Discussion

4.1. Microstructural analysis of SLM-EUROFER

In this chapter, microstructural features and precipitates of EUROFER97 produced by SLM will be discussed with reference to conventionally produced EUROFER97. For this purpose, EUROFER97 processed by SLM was analyzed in two different conditions: The condition right after SLM (SLM-EUROFER) as well as after post-processing in the form of HIP and subsequent heat treatments (SLM-EUROFER_HT, details in Tab. 2). For reference, studies on the effect of heat treatments, technological issues, and specific alloying elements on conventional EUROFER97 can be found, for example, in [17,21,28–32].

4.1.1. Grain size and shape of as-built SLM-EUROFER

The microstructural analysis by EBSD was performed on planes parallel to the build direction of the SLM process with two magnifications for an overview on the microstructure (500x) and a more detailed view of single grains (2000x). Fig. 1 shows inverse pole figure maps (IPF) and for SLM-EUROFER before post-processing (row one) and after post-processing (row two). For reference, an IPF map from EUROFER97 produced by conventional methods (casting, hot rolling, heat treatments) is included in the last row. Further analysis of misorientations inside grains allows to separate ferritic and martensitic grains [33] (details can be found in [14]).
Instead of the fully martensitic microstructure known from conventionally produced EUROFER97, the EUROFER97 processed by SLM (and before any heat treatment) exhibits ferritic grains as well as martensitic grains. The ferritic grains are elongated along the build direction with small-grained martensitic regions of different sizes in-between. The formation of such an inhomogeneous, bimodal microstructure can be attributed to the complex cooling conditions during the SLM processing, as the critical cooling rate for martensite formation depends on the volumetric energy density, the exposure strategy as well as the temperature of the former layers and is difficult to predict. The elongation of ferritic grains along the build direction can be attributed to the likewise oriented thermal gradient and is a typical feature for metals processed by SLM [34].
Applying HIP and subsequent heat treatments to EUROFER97 processed by SLM leads to successful removal of inhomogeneities and results in a uniform, fully martensitic microstructure (Fig. 1, row two). Further, SLM-processed EUROFER97 after post-processing (SLM-EUROFER_HT) also exhibit a qualitatively very similar microstructure to our reference material from a conventional production route (Fig. 1, last row).

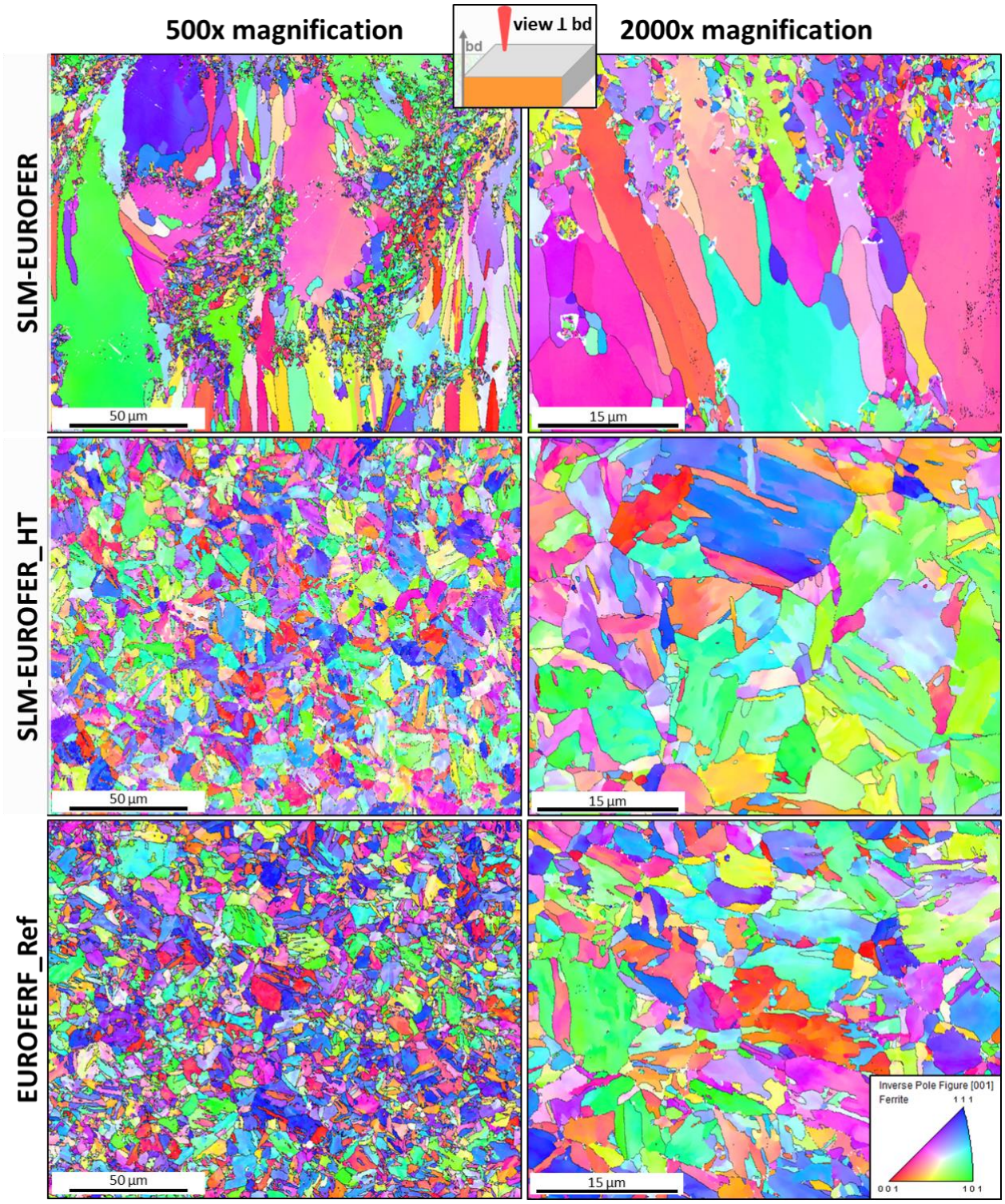

Fig. 1: Microstructure of SLM-EUROFER before and after post-processing (HIP and heat treatment), as well as for a reference sample prepared from conventionally produced EUROFER (EUROFER-Ref). The microstructure is imaged for an overview at 500x magnification and at 2000x for a more detailed view on single grains. Results are based on EBSD analyses from a plane perpendicular to the build direction and plotted in form of [001] IPF maps.

The quantitative evaluation in terms of grain size (in case of ferritic grains) and martensite packet size (in case of a martensitic microstructure) derived from multiple such EBSD maps confirms the

qualitative impression (Tab. 3). While SLM-EUROFER exhibits a large grain size of 15 µm with a high standard deviation due to the bimodal microstructure, the martensite packet size of the fully martensitic SLM-EUROFER_HT is with 6.42 merely slightly larger than conventionally produced EUROFER97 (EUROFER-Ref), 5.33 µm. The smaller dispersion of grain sizes in SLM-EUROFER_HT in comparison to SLM-EUROFER further indicates a homogenous microstructure.
SLM-EUROFER_HT exhibits a slightly larger hardness than the reference material, which seems to contradict the results regarding the martensite packet size, as a larger martensite packet size should result in a lower hardness. However, the SLM-EUROFER_HT was annealed at 750°C while the reference material from an earlier study was annealed at 780°C. The higher annealing temperature leads to fewer residual stresses and therefore to a lower hardness of the reference material. The same phenomena can explain the results for SLM-EUROFER before any heat-treatment, where the existing martensite is not annealed. This untempered martensite in the as-built condition leads to a nearly 100 HV2 higher hardness than for the other material conditions, even though roughly 50% of the microstructure is covered by large ferritic grains.

Tab. 3: Grain size (martensite packet size for martensitic microstructure) in terms of the average distance between high angle grain boundaries (> 15°) evaluated from EBSD analyses. Hardness from Vickers hardness tests (HV2). Grain size and hardness have been measured before post-processing (SLM-EUROFER), after HIP and heat treatments (SLM-EUROFER_HT) as well as for the reference material (EUROFER-Ref).

	martensite packet size, grain size	hardness
SLM-EUROFER	14.74 ± 4.52 µm	336 ± 11 HV2
SLM-EUROFER_HT	6.42 ± 0.68 µm	252 ± 3 HV2
EUROFER-Ref	5.33 µm	252 HV2

From a technological point of view, it is important to emphasize that in defiance of the inhomogeneous condition after the SLM production, the grain size and shape after post-processing is qualitatively similar to conventionally produced EUROFER97. Earlier studies showed that this is also true for different wall thicknesses down to 500 µm [14]. The fact that inhomogeneities of grain size and shape, as well as the partly ferritic nature of grains in the initial state after SLM production, can be tailored by conventional heat treatments towards a typical EUROFER97 microstructure, will be an important fact for future qualification of the selective laser melting process.

4.1.2. Precipitates in SLM-EUROFER

Small-scale microstructural features, as the martensite lath width and the kind, size and distribution of precipitates, are known to influence mechanical properties in RAFM 9%-Cr steels [25]. To evaluate their influence in EUROFER97 fabricated by SLM, a TEM-study was performed on batch-2 in the as-built state as well as after post-processing.
Fig. 2 shows two STEM-EDX elemental mappings of additively manufactured samples. There are marked differences visible between the as-built (SLM-EUROFER) and the post-processed (SLM-EUROFER_HT) condition. In the STEM-EDX maps of the as-built condition, only a uniform contrast is recognized, i.e., all grains have the same composition. This is a distinct difference to conventionally manufactured EUROFER97 samples (EUROFER_Ref), where besides the Fe-Cr

matrix also $M_{23}C_6$ and MX-type precipitate phases are present. The absence of these two precipitate phases might negatively affect the mechanical performance of the as-built EUROFER97. Therefore, in order to improve the mechanical performance of additively manufactured EUROFER97 samples, hot isostatic pressing (HIP) and subsequent heat treatments were applied. The result of additive manufactured EUROFER97 after post-processing is presented in Fig. 2 (SLM-EUROFER_HT). Here, both precipitate phases – $M_{23}C_6$ and MX – were observed and are located predominately at boundaries, i.e., prior austenite grain boundaries, lath and package boundaries. For $M_{23}C_6$ precipitates, this is in good agreement to conventionally manufactured EUROFER97 (Fig. 2, EUROFER_Ref). However, from a qualitative impression, MX precipitates seem to be more uniformly distributed in EUROFER_Ref than in SLM-EUROFER_HT, where we find a higher concentration at boundaries. The agglomeration of precipitates at grain boundaries could explain the lower toughness of SLM-EUROFER-HT in comparison to EUROFER_Ref, as demonstrated in a former publication using the same material [14].
The chemical composition of the precipitate phases are qualitatively the same as in conventional EUROFER97, i.e. $M_{23}C_6$ contains Cr, W and a small amount of V in the M-part of the phase and MX is here (V, Ta)N. However, what is still different to conventionally manufactured EUROFER97 is the presence of a few about 600 nm sized elongated precipitates that contain V, Ta and Cr in similar concentrations as well as about 5 times less N and W. Some MnS particles were observed, but their number density is negligible (see supplementary, Fig. S1).

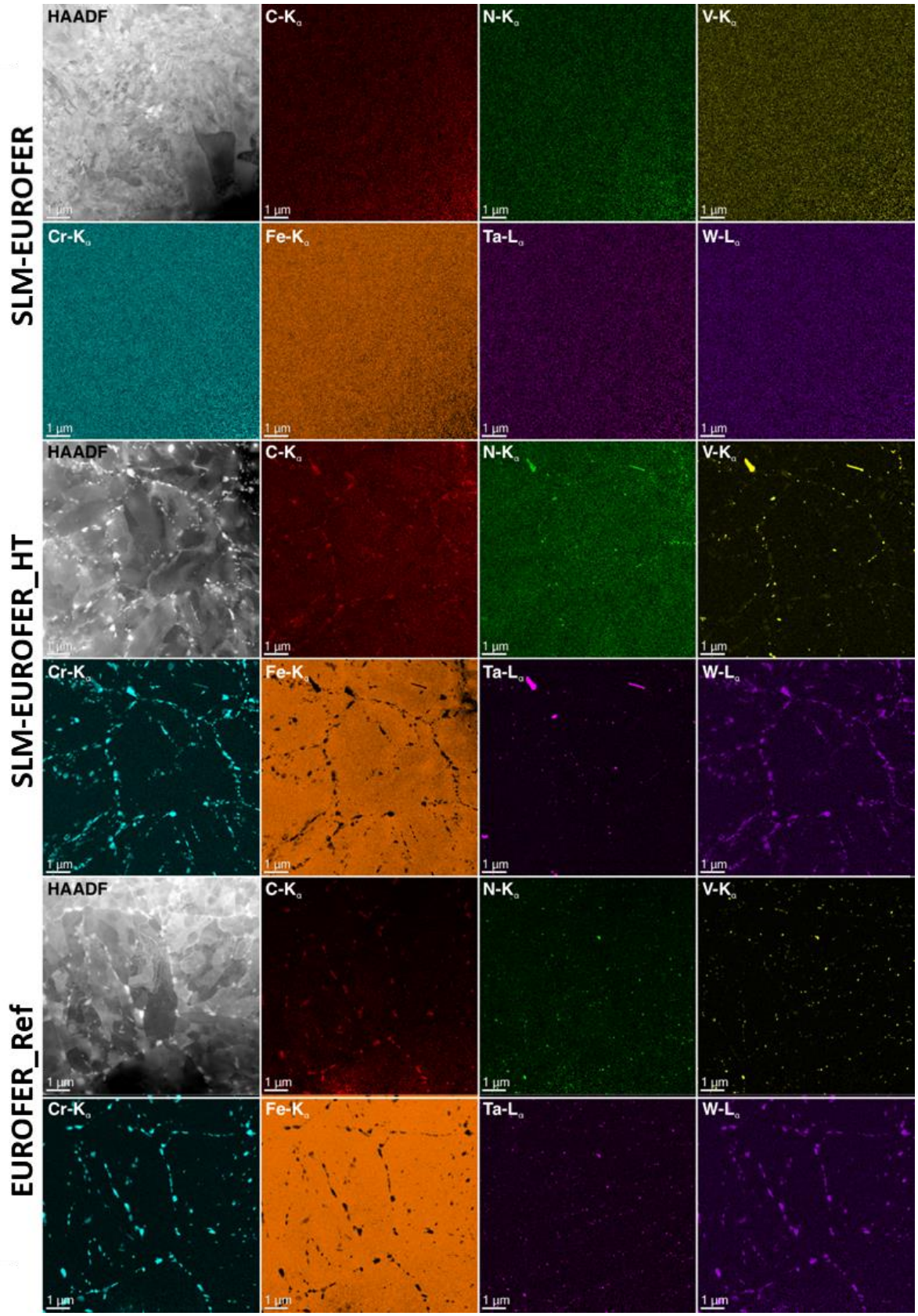

Fig. 2: STEM-EDX elemental mappings of an additively manufactured EUROFER97 sample in the as-built condition (SLM-EUROFER), and after HIP and heat treatment (SLM-EUROFER_HT), as well as of a conventionally fabricated EUROFER97 (EUROFER_Ref).

Fig. 3 deals with a detailed analysis of the thermally stable MX-type nano-precipitates in SLM-EUROFER97 after post-processing (SLM-EUROFER_HT), which are important for the high-temperature strength of EUROFER97. Elements Al and Zr were considered as well, since both elements form nano-sized precipitates in this SLM-EUROFER batch that have a non-negligible volume density (see Tab. 4). Fig. 3 shows that MX-type precipitates divide into multiple types: (i) V nitrides and (ii) Ta carbonitrides, (iii) Al oxides, and (iv) Zr oxides. The nitrides and carbonitrides particle sizes range from about 20 nm to 100 nm. The oxide particles have sizes in the range of about 10 nm to 40 nm, assessable by the small bright blue areas in the oxygen map which coincide with the bright areas in the Al- and Zr-maps. In some cases, both types of particles form agglomerates. The left half of the STEM-HAADF image reveals dislocations that are attached to MX-type particles, proving their relevance as active pinning sites, which is also known in conventionally processed EUROFER97 samples or oxide-strengthened steels (ODS). A higher resolution image is provided in Fig. S2. The oxide-type precipitates were not observed in conventionally processed EUROFER97 samples. From the magnified regions of the Cr and W elemental map, which are displayed at the bottom right of Fig. 3, another interesting feature in form of a high local content of Cr and W at the grain boundary can be seen. However, the carbon map is too noisy to clarify if these Cr- and W-atoms form precipitates or if this is an indication for grain boundary diffusion towards the $M_{23}C_6$ precipitates located at the left and right of both maps.

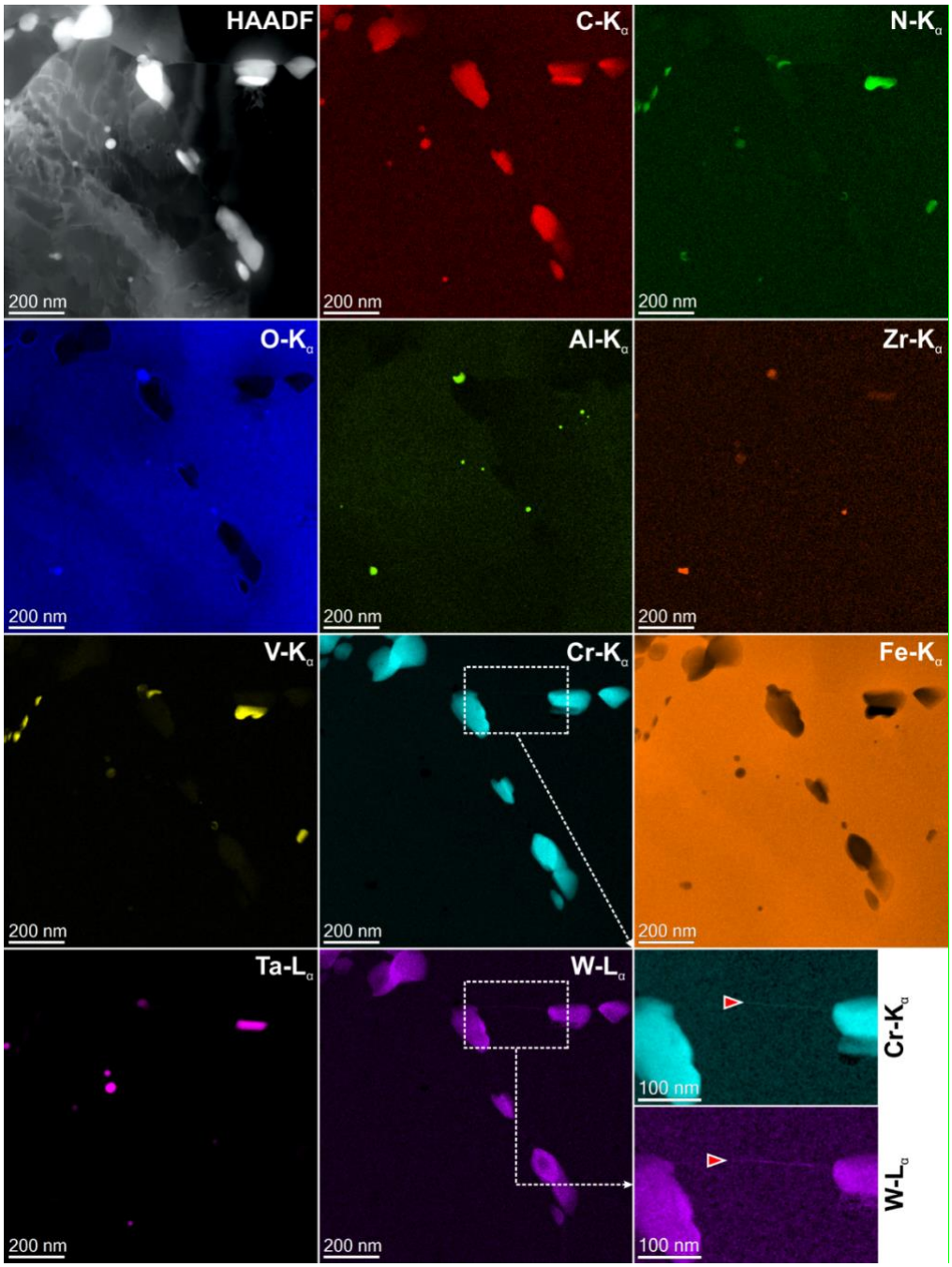

Fig. 3: STEM-EDX mapping of an additively manufactured EUROFER97 sample after HIP and heat treatment (SLM-EUROFER_HT) at high magnification. The magnified Cr and W elemental maps indicate Cr and W enrichment along grain boundaries (see red triangle).

In order to get a quantitative comparison of the precipitates population between conventionally manufactured (EUROFER_Ref) and additively manufactured EUROFER97 samples (SLM-EUROFER_HT), STEM-EDX maps were evaluated with respect to precipitate size and volume density. The results are summarized in Tab. 4. All types of precipitates have a log-normal distribution of grain sizes (see supplementary, Fig. S3). In the case of the SLM-EUROFER_HT sample, the mean precipitate size (138 nm) is significantly smaller than for the EUROFER_Ref sample (176 nm). In addition, the outliers reach larger grain size values for the reference sample. The grain sizes of the MX-type precipitates exhibit a similar trend as the $M_{23}C_6$ precipitates, i.e.,

the MX precipitates of additively manufactured EUROFER97 are about 10-15 nm smaller on average than those of conventionally produced EUROFER97.
Moreover, the precipitate volume densities were determined for both sample types and summarized in Tab. 4. The volume densities of all precipitates lie in the same order of magnitude, i.e., 10^{19} particles per m^3. The $M_{23}C_6$ volume density in the SLM-EUROFER_HT sample is approximately twice the value of the reference material. In the case of the MX-type precipitates, marked differences were observed between both samples. In EUROFER_Ref, Ta and V form in most cases a combined carbonitride. For the SLM-EUROFER_HT sample, the volume density values of the MX-type phases are always less than for the reference material, however, a clear separation into V nitrides and Ta carbonitrides was observed. In addition, in the additively manufactured case, also Al and Zr oxides are present with a volume density comparable to the Ta- and V-rich precipitates. Thus, the combined volume density of MX-precipitates, which are of importance as dislocation-pinning sites, is about the same for the additively manufactured as for the conventionally produced EUROFER97 sample. In summary, SLM-EUROFER_HT shows an overall larger number of precipitates in comparison to EUROFER_Ref, which could explain the higher strength and lower ductility of SLM-EUROFER_HT observed in tensile tests (see publication using the same material [14]).

Tab. 4: Number of particles analyzed, volume density and particle size in terms of Feret's diameter of precipitates for additively and conventionally processed EUROFER97. Particle size distributions can be found in the supplementary material (Fig. S3). All precipitate size distributions are log-normal.

Sample		$M_{23}C_6$	MX Ta-rich	MX V-rich	MX Al-rich	MX Zr-rich
SLM-EUROFER_HT	Particle count	789	54	86	65	41
	Vol.-density (m^{-3})	$5.63\ 10^{19}$	$3.56\ 10^{19}$	$5.66\ 10^{19}$	$4.28\ 10^{19}$	$2.70\ 10^{19}$
	Particle size (nm)	138 ± 167	33 ± 50	35 ± 57	22 ± 18	21 ± 120
EUROFER_Ref	Particle count	426	83	83	--	--
	Vol.-density (m^{-3})	$3.26\ 10^{19}$	$7.40\ 10^{19}$	$7.40\ 10^{19}$	--	--
	Particle size (nm)	176 ± 256	42 ± 51	50 ± 70	--	--

In order to assess the phases being present in Fig. 3, the STEM-EDX dataset was treated by principal component analysis (PCA) assuming Poisson noise. The algorithm sorts the main components of the dataset according to their proportion of variance (see Fig. 4, Scree plot). In the case of STEM-EDX, all principal components left of the dashed line in the Scree plot are considered as relevant. These principal components are decomposed into two datasets: the first one is in the navigation space (labeled as loading) and the second one is in the signal space (labeled as factor). In the present case, the loadings show the spatial distribution of each phase, whereas the factors are used to determine the elements being present in each phase and, thus, the phase itself, e.g., $M_{23}C_6$ or MX. Please note that the coloring of phases in Fig. 4 is in contrast to Fig. 3, where single elemental maps are presented. Six distinct phases were found and are shown in Fig. 4. The first phase corresponds to the Fe/Cr matrix , the second one represents the $M_{23}C_6$ phase, i.e. $(Cr, W)_{23}C_6$, the third one is TaC, the fourth one is VN, the fifth one corresponds to a surface oxide, and the last one consists of Al- and Zr-oxides. Hence, it became evident from Fig. 4 that in the additively manufactured and post-processed EUROFER97, the MX-type precipitates can be separated into two distinct types of phases, i.e., VN and TaC.

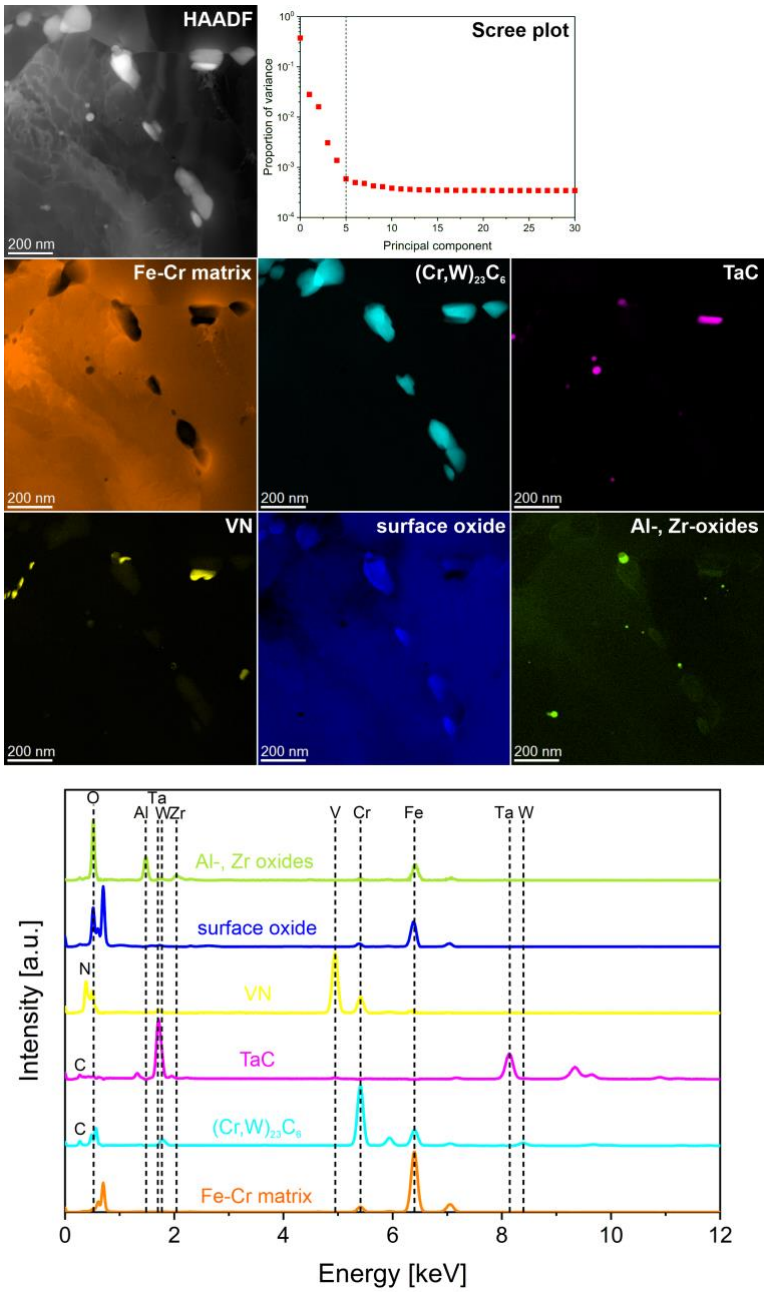

Fig. 4: Decomposition of the STEM-EDX data presented in Figure 2 via non-negative matrix factorization as implemented in the Hyperspy package [27] revealing the present phases.

In summary, the TEM investigations reveal that additively manufactured EUROFER97 needs to be post-processed to develop the necessary microstructure for improved mechanical performance, i.e., the $M_{23}C_6$ and MX-type precipitates. It became also evident that the precipitate sizes, as well as their density, are improved (or at least equal) in the additively manufactured EUROFER97 compared to the reference material from the conventional production route and are thus not the limiting factor of the mechanical performance. The only significant differences are the presence of a few ~600 nm sized elongated precipitates that contain V, Ta and Cr, the apparent concentration of MX-precipitates on grain boundaries, the diffusion of Cr and W along grain boundaries, and the presence of nano-sized Al and Zr oxides in the AM sample. However, the presence of nano-sized oxide precipitates should even increase the mechanical performance of the material, as it is, for example, the case in ODS-type steels.

5. Conclusions

In this work, the key microstructural characteristics of EUROFER97 fabricated by selective laser melting (SLM) from pre-alloyed powder, and how to adapt them by adequate post-processing, were investigated by studying SLM-EUROFER97 in its initial state after fabrication as well as after different post-processing steps. Referring to the main questions stated in the introduction (section 1), we can conclude the following:

(1) What are the microstructural characteristics of EUROFER97 processed by SLM with regard to grain size and shape?
EUROFER97 after fabrication by SLM and without further treatment (SLM-EUROFER) does not show the typical fully martensitic microstructure as desired, but rather a peculiar bimodal microstructure of both untempered martensite as well as large ferrite grains elongated in build direction (see Fig. 1).

(4) Do both $M_{23}C_6$ and MX type precipitates form homogeneously distributed in EUROFER97 processed by SLM?
The analysis of precipitates emphasizes the risk of following a powder-metallurgical route: EUROFER97 processed by SLM does not reveal precipitates, as their formation is most probably suppressed by the high cooling rates during the SLM process – at least for the parameter set used for the production of this batch (104 J/mm^3 volumetric energy density).

(2) If necessary, how can the microstructure be altered to a microstructure comparable to one of conventionally fabricated EUROFER97?
Submitting EUROFER97 processed by SLM to appropriate post-processing consisting of hot isostatic pressing, austenitization, quenching and tempering, allows tuning the inhomogeneous microstructure described above to a uniform microstructure rather similar to the microstructure of conventionally produced EUROFER97. The microstructure consists then of fully martensitic grains with a uniform grain shape and an average martensite packet size of 6.42 µm, which is only slightly larger than the 5.33 µm of conventional EUROFER97.
Further, the performed post-processing leads to the formation of $M_{23}C_6$ and MX precipitates with a similar volume density and an even smaller size than precipitates formed in conventional EUROFER97. Additionally, nano-sized oxides from contaminations during the atomization process were detected and the chemical composition of the precipitates shows slight deviations compared to the conventionally produced EUROFER97, but those deviations are not expected to influence the mechanical properties.

The microstructural analysis confirms the need for adequate heat treatments of EUROFER97 processed by SLM to achieve a uniform, fully martensitic microstructure as well as the formation of $M_{23}C_6$ and MX precipitates.

SUPPLEMENTARY

Tab. S 1: Chemical composition (wt.-%) of the raw material, the atomized pre-alloyed powder and the respective SLM parts fabricated with this powder (SLM-EUROFER). Further, the chemical composition (wt.-%) of the reference material and the specifications for EUROFER97 are given.

(wt.-%)	Cr	C	Mn	V	W	Ta	N	O
raw material	8.73	0.11	0.019	0.35	1.08	0.092	0.042	0.0052
pre-alloyed powder	9.46	0.1	0.021	0.35	1.10	0.090	0.025	0.022
SLM-EUROFER	9.39	0.09	0.019	0.36	1.12	0.094	0.0254	0.0065
EUROFER_Ref	9.36	0.095	0.501	0.19	1.21	0.1	0.0067	0.0104
EUROFER_Spec	8.5-9.5	0.09-0.12	0.2-0.6	0.15-0.25	1.0-1.2	0.05-0.09	0.015-0.045	< 0.01

(wt.-%)	Cu	Ni	Si	S	B	Ti	Al	Mo
raw material	0.0072	0.0036	0.036	0.0011	$< 5 \cdot 10^{-4}$	$<1 \cdot 10^{-4}$	0.0014	$<9 \cdot 10^{-4}$
pre-alloyed powder	0.007	0.006	0.039	$<2 \cdot 10^{-3}$	0.017	0.0002	0.0037	0.0014
SLM-EUROFER	0.01	0.009	0.039	$<2 \cdot 10^{-3}$	0.017	0.0002	0.0034	0.0024
EUROFER_Ref	0.007	/	0.033	0.0017	/	0.1	<0.001	0.0024
EUROFER_Spec	< 0.005	< 0.005	< 0.05	< 0.005	< 0.001	< 0.01	< 0.01	< 0.005

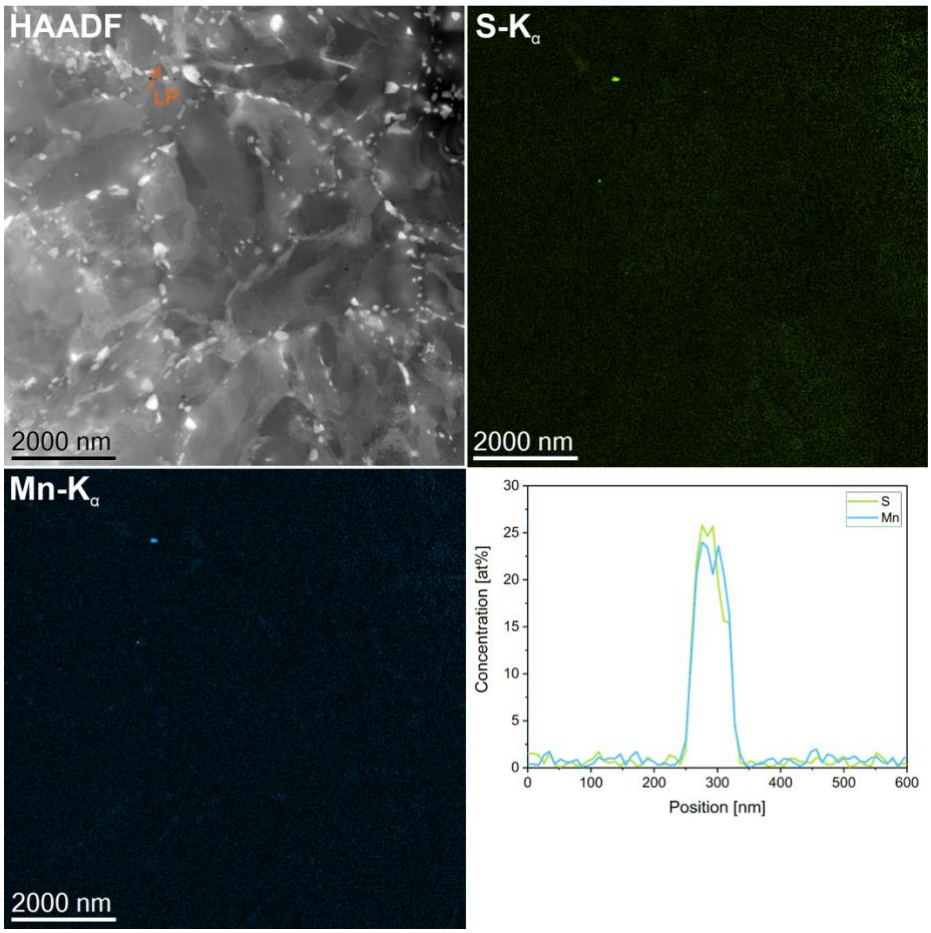

Fig. S1: STEM-EDX elemental mappings for manganese (Mn) and sulfur (S) of additively manufactured EUROFER97 after HIP and heat treatment (SLM-EUROFER_HT), supplementing FIG. 2).

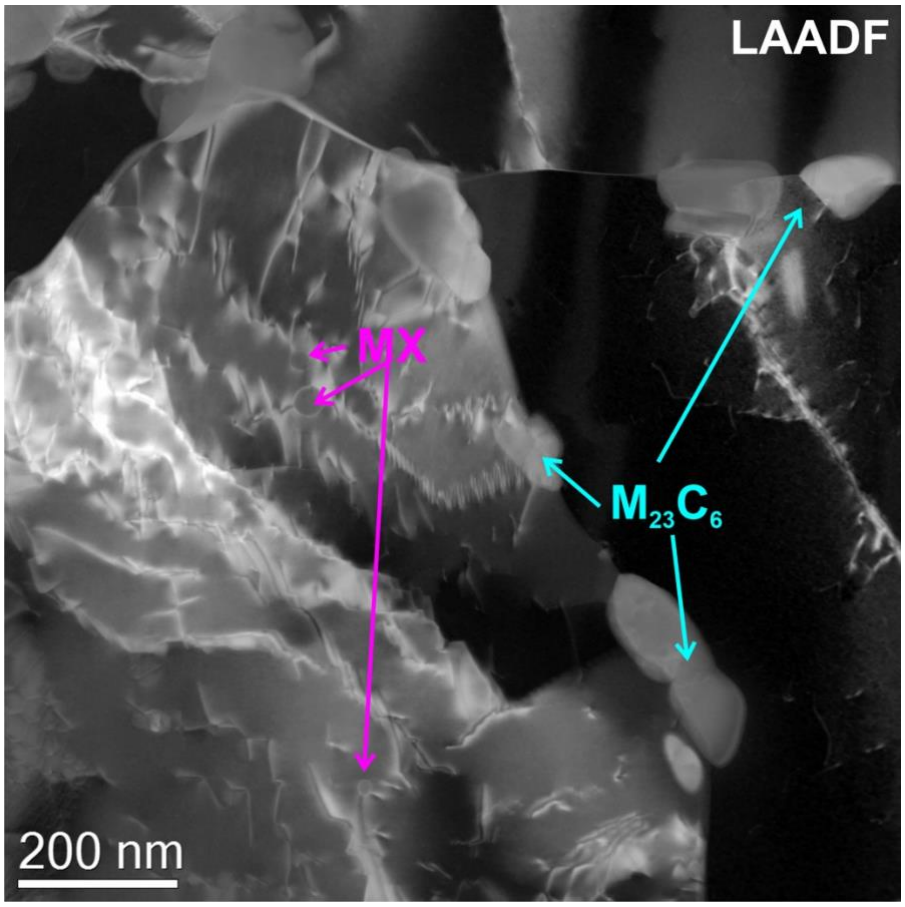

Fig. S2: Higher magnification of section from Fig. 3, using low-angle annular dark-field imaging (LAADF) to illustrate the pinning of dislocations by MX-precipitates.

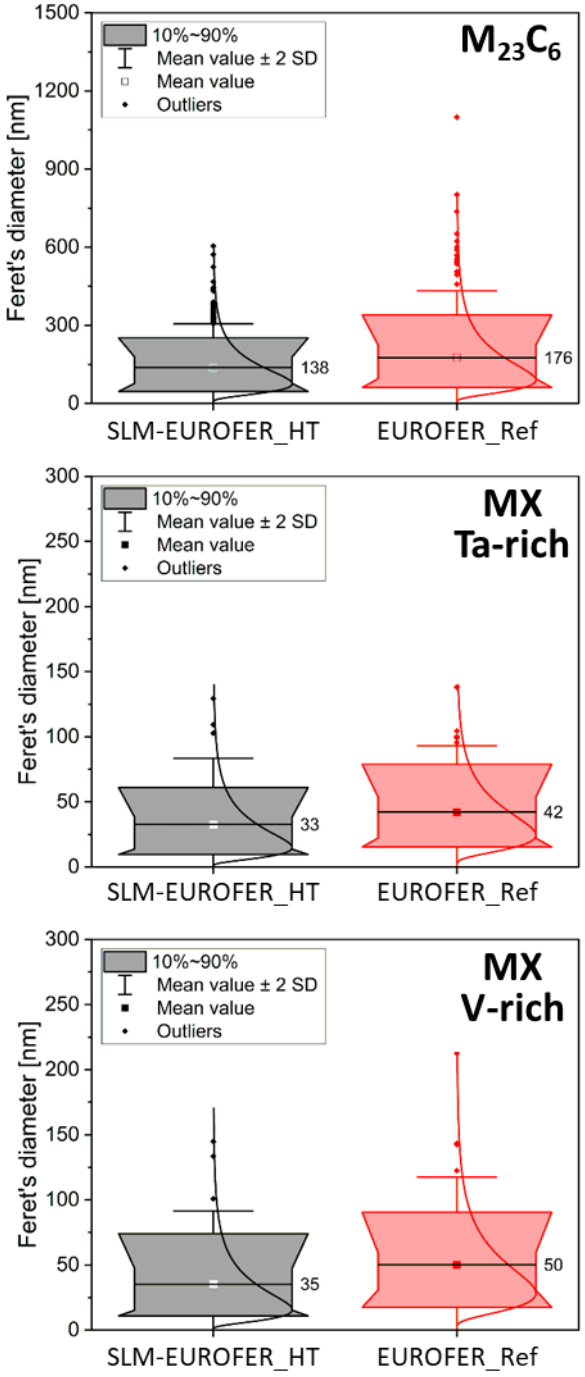

Fig. S3: Grain size evaluation of the $M_{23}C_6$ (a) Ta-rich, (b) and V-rich MX phase for additively manufactured and post-processed (SLM-EUROFER_HT) as well as conventionally manufactured (EUROFER-Ref) EUROFER97. All precipitates are log-normally distributed.

Acknowledgements
This work has been carried out within the framework of the EUROfusion Consortium and has received funding from the Euratom Research and Training Programme 2014-2018 and 2019-2020 under grant agreement No 633053. The views and opinions expressed herein do not necessarily reflect those of the European Commission. The support of Rosswag GmbH, the contractor for powder atomization and selective laser melting, is gratefully acknowledged. We are thankful for specimen preparation and mechanical testing by Tanja Fabry, Siegfried Baumgärtner and Daniel Bolich. Special thanks go to Margarete Offermann (IAM-ESS) for the powder characterization and to the group of Thomas Bergfeldt (IAM-AWP) for the chemical analysis.

Data availability
The raw/processed data required to reproduce these findings cannot be shared at this time as the data also form part of an ongoing study.

References
[1] B. Dutta, S. Babu, B. Jared, Science, technology and applications of metals in additive manufacturing, Elsevier, Amsterdam (2019).
[2] N. Ordás, L.C. Ardila, I. Iturriza, F. Garcianda, P. Álvarez, C. García-Rosales, Fabrication of TBMs cooling structures demonstrators using additive manufacturing (AM) technology and HIP, Fusion Eng. Des. 96-97 (2015) 142–148. http://dx.doi.org/10.1016/j.fusengdes.2015.05.059.
[3] Y. Zhong, L.-E. Rännar, S. Wikman, A. Koptyug, L. Liu, D. Cui, Z. Shen, Additive manufacturing of ITER first wall panel parts by two approaches: Selective laser melting and electron beam melting, Fusion Eng. Des. 116 (2017) 24–33. http://dx.doi.org/10.1016/j.fusengdes.2017.01.032.
[4] H. Neuberger, J. Rey, M. Hees, E. Materna-Morris, D. Bolich, J. Aktaa, A. Meier et al., Selective Laser Sintering as Manufacturing Process for the Realization of Complex Nuclear Fusion and High Heat Flux Components, Fusion Sci. Technol. 72 (2017) 667–672. http://dx.doi.org/10.1080/15361055.2017.1350521.
[5] C. Koehly, H. Neuberger, L. Bühler, Fabrication of thin-walled fusion blanket components like flow channel inserts by selective laser melting, Fusion Eng. Des. 143 (2019) 171–179. http://dx.doi.org/10.1016/j.fusengdes.2019.03.184.
[6] M.J. Gorley, Critical Assessment 12: Prospects for reduced activation steel for fusion plant, Mater. Sci. Technol. 31 (2015) 975–980. http://dx.doi.org/10.1179/1743284714Y.0000000732.
[7] A. Alamo, J.L. Bertin, V.K. Shamardin, P. Wident, Mechanical properties of 9Cr martensitic steels and ODS-FeCr alloys after neutron irradiation at 325°C up to 42dpa, J. Nucl. Mater. 367-370 (2007) 54–59. http://dx.doi.org/10.1016/j.jnucmat.2007.03.166.
[8] W.E. Frazier, Metal Additive Manufacturing: A Review, J. Mater. Eng. Perform. 23 (2014) 1917–1928. http://dx.doi.org/10.1007/s11665-014-0958-z.
[9] I. Gibson, D.W. Rosen, B. Stucker, Additive manufacturing technologies: 3D printing, rapid prototyping and direct digital manufacturing, 2nd ed., Springer, New York (2015).
[10] J.H.K. Tan, S.L. Sing, W.Y. Yeong, Microstructure modelling for metallic additive manufacturing: a review, Virtual and Physical Prototyping 15 (2020) 87–105. http://dx.doi.org/10.1080/17452759.2019.1677345.
[11] C. Haase, J. Bültmann, J. Hof, S. Ziegler, S. Bremen, C. Hinke, A. Schwedt et al., Exploiting Process-Related Advantages of Selective Laser Melting for the Production of High-Manganese Steel, Materials 10 (2017). http://dx.doi.org/10.3390/ma10010056.
[12] L.E. Murr, E. Martinez, J. Hernandez, S. Collins, K.N. Amato, S.M. Gaytan, P.W. Shindo, Microstructures and Properties of 17-4 PH Stainless Steel Fabricated by

Selective Laser Melting, J. Mater. Res. Technol. 1 (2012) 167–177. http://dx.doi.org/10.1016/S2238-7854(12)70029-7.
[13] C.S. Wright, M. Youseffi, S.P. Akhtar, T.H.C. Childs, C. Hauser, P. Fox, Selective Laser Melting of Prealloyed High Alloy Steel Powder Beds, Mater. Sci. Forum 514-516 (2006) 516–523. http://dx.doi.org/10.4028/www.scientific.net/MSF.514-516.516.
[14] S. Bonk, H. Neuberger, D. Beckers, J. Koch, S. Antusch, M. Rieth, Additive manufacturing technologies for EUROFER97 components, J. Nucl. Mater. 548 (2021). https://doi.org/10.1016/j.jnucmat.2021.152859
[15] R.L. Klueh, Heat treatment behavior and tensile properties of Cr−W steels, MTA 20 (1989) 463–470. http://dx.doi.org/10.1007/BF02653926.
[16] R.L. Klueh, E.T. Cheng, M.L. Grossbeck, E.E. Bloom, Impurity effects on reduced-activation ferritic steels developed for fusion applications, J. Nucl. Mater. 280 (2000) 353–359. http://dx.doi.org/10.1016/S0022-3115(00)00060-X.
[17] H. Tanigawa, M.A. Sokolov, A. Sawahata, N. Hashimoto, M. Ando, K. Shiba, M. Enomoto et al., Effect of Ta Rich Inclusions and Microstructure Change During Precracking on Bimodal Fracture of Reduced-Activation Ferritic/Martensitic Steels Observed in Transition Range, J. ASTM Int. 6 (2009) 101728. http://dx.doi.org/10.1520/JAI101728.
[18] R.L. Klueh, W.R. Corwin, Impact behavior of Cr-W steels, J. Materials Engineering 11 (1989) 169–175. http://dx.doi.org/10.1007/BF02834465.
[19] R.L. Klueh, P.J. Maziasz, The microstructure of chromium-tungsten steels, MTA 20 (1989) 373–382. http://dx.doi.org/10.1007/BF02653916.
[20] R.L. Klueh, D.J. Alexander, M.A. Sokolov, Effect of rhenium and osmium on mechanical properties of a 9Cr–2W–0.25V–0.07Ta–0.1C steel, Journal of Nuclear Materials 279 (2000) 91–99. http://dx.doi.org/10.1016/S0022-3115(99)00269-X.
[21] R.L. Klueh, D.J. Alexander, M.A. Sokolov, Effect of chromium, tungsten, tantalum, and boron on mechanical properties of 5–9Cr–WVTaB steels, Journal of Nuclear Materials 304 (2002) 139–152. http://dx.doi.org/10.1016/S0022-3115(02)00885-1.
[22] D. Herzog, V. Seyda, E. Wycisk, C. Emmelmann, Additive manufacturing of metals, Acta Mater. 117 (2016) 371–392. http://dx.doi.org/10.1016/j.actamat.2016.07.019.
[23] Z. Dong, X. Zhang, W. Shi, H. Zhou, H. Lei, J. Liang, Study of Size Effect on Microstructure and Mechanical Properties of AlSi10Mg Samples Made by Selective Laser Melting, Materials 11 (2018) 2463. http://dx.doi.org/10.3390/ma11122463.
[24] C. Phutela, N.T. Aboulkhair, C.J. Tuck, I. Ashcroft, The Effects of Feature Sizes in Selectively Laser Melted Ti-6Al-4V Parts on the Validity of Optimised Process Parameters, Materials 13 (2019). http://dx.doi.org/10.3390/ma13010117.
[25] J. Hoffmann, M. Rieth, L. Commin, P. Fernández, M. Roldán, Improvement of reduced activation 9%Cr steels by ausforming, Nucl. Mater. Energy 6 (2016) 12–17. http://dx.doi.org/10.1016/j.nme.2015.12.001.
[26] J. Hoffmann, M. Rieth, M. Klimenkov, S. Baumgärtner, Improvement of EUROFER's mechanical properties by optimized chemical compositions and thermo-mechanical treatments, Nucl. Mater. Energy 16 (2018) 88–94. http://dx.doi.org/10.1016/j.nme.2018.05.028.
[27] F.D. La Peña, E. Prestat, V.T. Fauske, P. Burdet, P. Jokubauskas, M. Nord, T. Furnival et al., hyperspy/hyperspy: HyperSpy 1.6.0, Zenodo (2020).
[28] L. Tan, D.T. Hoelzer, J.T. Busby, M.A. Sokolov, R.L. Klueh, Microstructure control for high strength 9Cr ferritic–martensitic steels, Journal of Nuclear Materials 422 (2012) 45–50. http://dx.doi.org/10.1016/j.jnucmat.2011.12.011.
[29] R.L. Klueh, P.J. Maziasz, D.J. Alexander, Heat-treatment effect on impact properties of reduced-activation steels, Journal of Nuclear Materials 179-181 (1991) 679–683. http://dx.doi.org/10.1016/0022-3115(91)90180-F.

[30] N. Baluc, D.S. Gelles, S. Jitsukawa, A. Kimura, R.L. Klueh, G.R. Odette, B. van der Schaaf et al., Status of reduced activation ferritic/martensitic steel development, Journal of Nuclear Materials 367-370 (2007) 33–41. http://dx.doi.org/10.1016/j.jnucmat.2007.03.036.
[31] R.L. Klueh, N. Hashimoto, M.A. Sokolov, Effect of Heat Treatment and Tantalum on Microstructure and Mechanical Properties of Fe-9Cr-2W-0.25V Steel, in: M.L. Grossbeck, T.R. Allen, R.G. Lott, A.S. Kumar (Eds.), Effects of Radiation on Materials: 21st International Symposium, ASTM International, 100 Barr Harbor Drive, PO Box C700, West Conshohocken, PA 19428-2959 (2004) 376-376-15. http://dx.doi.org/10.1520/STP11241S.
[32] H. Tanigawa, T. Hirose, K. Shiba, R. Kasada, E. Wakai, H. Serizawa, Y. Kawahito et al., Technical issues of reduced activation ferritic/martensitic steels for fabrication of ITER test blanket modules, Fusion Eng. Des. 83 (2008) 1471–1476. http://dx.doi.org/10.1016/j.fusengdes.2008.07.024.
[33] N. Peranio, Y.J. Li, F. Roters, D. Raabe, Microstructure and texture evolution in dual-phase steels: Competition between recovery, recrystallization, and phase transformation, Mater. Sci. Eng. A 527 (2010) 4161–4168. http://dx.doi.org/10.1016/j.msea.2010.03.028.
[34] N. Ahmed, Direct metal fabrication in rapid prototyping: A review, J. Manuf. Process. 42 (2019) 167–191. http://dx.doi.org/10.1016/j.jmapro.2019.05.001.